RAPID COMMUNICATION

Conductive path and local oxygen-vacancy dynamics: Case study of crosshatched oxides

Z W Liang(梁正伟)[1,2], P Wu(吴平)[1], L C Wang(王利晨)[2,4], B G Shen(沈保根)[2,3,4,5], and Zhi-Hong Wang(王志宏)[2,†]

[1] *Department of Physics, University of Science and Technology Beijing, Beijing* 100083, *China*
[2] *Beijing National Laboratory for Condensed Matter Physics, Institute of Physics, Chinese Academy of Sciences, Beijing* 100190, *China*
[3] *School of Physical Sciences, University of Chinese Academy of Sciences, Beijing* 101408, *China*
[4] *Ningbo Institute of Materials Technology & Engineering, Chinese Academy of Sciences, Ningbo* 315201, *China*
[5] *Ganjiang Innovation Academy, Chinese Academy of Sciences, Ganzhou* 341000, *China*

(Received 20 November 2022; revised manuscript received 15 January 2023; accepted manuscript online 18 January 2023)

By employing scanning probe microscopy, conductive path and local oxygen-vacancy dynamics have been investigated in crosshatched $La_{0.7}Sr_{0.3}MnO_3$ thin films grown onto flat and vicinal $LaAlO_3$(001) single crystal substrates. Consistent with prior studies, the crosshatch topography was observed first by dynamical force microscopy as the epi-stain started to release with increasing film thickness. Second, by using conductive atomic force microscopy (CAFM), conductive crosshatch and dots (locally aligned or random) were unravelled, however, not all of which necessarily coincided with that shown in the *in situ* atomic force microscopy. Furthermore, the current–voltage responses were probed by CAFM, revealing the occurrence of threshold and/or memristive switchings. Our results demonstrate that the resistive switching relies on the evolution of the local profile and concentration of oxygen vacancies, which, in the crosshatched films, are modulated by both the misfit and threading dislocations.

Keywords: resistive switching, oxygen-vacancy dynamics, crosshatch, dislocation, scanning probe microscopy

PACS: 73.63.–b, 68.37.–d, 61.72.Yx, 72.80.–r **DOI:** 10.1088/1674-1056/acb421

1. Introduction

Recently, functional defects have received renewed attention due to their pivotal role in controlling phase of matter and fostering new device paradigms.[1–4] Of particular interest, electrically tuning the profile and concentration of oxygen vacancies causes resistive switching (RS) phenomenon,[5–8] which finds promising applications in nonvolatile memories and neuromorphic computing.[9–11] Despite the focus of intense research activity, the oxygen-vacancy dynamics for RS is not yet fully explored. The challenges include, but not limited to probing and understanding the local vacancy behavior. On the one side, the RS devices are commonly sandwiched with deposited electrodes in macro-size, making it difficult to observe the local vacancy behavior both along the lateral direction and at the metal–oxide interface. On the other side, apart from oxygen vacancies, other defects such as misfit and threading dislocations often present in oxide heterostructures. However, to date, the interplay between these extended defects and oxygen vacancies remains largely elusive.

In this work, we aim to tackle these issues through studying the local oxygen-vacancy dynamics in crosshatched $La_{0.7}Sr_{0.3}MnO_3$ (LSMO) thin films by using conductive atomic force microscopy (CAFM). As a salient pattern, crosshatch has been observed in heteroepitaxies of semiconductors[12–16] and complex perovskite oxides.[17–21] It is in general along crystallographic directions, and mainly controlled by ordered misfit dislocations that propagate and interact as the misfit strain begins to release. The recent studies mostly from theoretical aspects point out that the dislocation core enables a preferential absorption of oxygen vacancies.[22–27] Accordingly, the crosshatched films would provide a unique platform for clarifying the local oxygen-vacancy behavior down to nanoscales.

2. Experiment

The LSMO thin films with thickness of $\sim$ 22 nm and 80 nm were grown onto flat and vicinal $LaAlO_3$ (LAO)(001) single crystal substrates by using 90° off-axis rf magnetron sputtering.[28] The vicinal LAO(001) was miscut by 5° off the (001) plane toward [010].[28,29] The vicinal substrates were employed in order to study the case when the strain relaxation and consequently the creation of dislocations were further affected by the coherent atomic steps on the substrate surface.[30] The film samples hereinafter are referred to as $\mathcal{FS}$-t and $\mathcal{VS}$–t ($\mathcal{FS}$: flat substrate, $\mathcal{VS}$: vicinal substrate, and t: film thickness). The magnetron sputtering was performed at

†Corresponding author. E-mail: z.wang@iphy.ac.cn
© 2023 Chinese Physical Society and IOP Publishing Ltd

a power of 70 W and a pressure of 2.0 Pa (Ar:O_2 ~ 3 : 1) from a base less than 3.3×10^{-5} Pa. The ceramic target in 2 inch diameter was prepared by spark plasma sintering.[31] The substrate temperature (T_S) was kept at about 840 °C. This somewhat high T_S was employed, as we learned from the prior work that a high T_S appears to favor the formation of surface crosshatching.[19] After the deposition, the films were *in situ* annealed at an oxygen pressure of 500 Pa for 20 min.

The x-ray diffraction was carried out on a Bruker x-ray diffractometer (D8 Discover) with Cu $K\alpha$ radiation. The scanning electron microscopy (SEM) with x-ray energy dispersive spectroscopy (EDS) was performed on a Hitachi S-4800 scanning electron microscope. The x-ray absorption spectra were measured in total electron yield mode at the beam line 08U1A of Shanghai Synchrotron Radiation Facility (SSRF). The Raman spectroscopy was measured in normal backscattering geometry with the excitation line in wavelength of 532 nm of Nd:YAG solid-state laser, by using a micro-Raman spectrometer (Horiba/Jobin Yvon HR800). The thermomagnetization curves were measured using a Quantum Design superconducting quantum interference device (SQUID) vibrating sample magnetometer (VSM).

The topographical and electrical measurements were performed at room temperature by using a scanning probe microscope (SEIKO SPI3800N) including functions of dynamical force microscopy (DFM), atomic force microscopy (AFM) and CAFM. It is noteworthy that, as a non-contact technique, DFM employs an oscillating tip to scan the topography by maintaining a constant interaction between tip and sample, while CAFM is a contact technique using a metallic tip, and sensing the sample currents with a constant electrical bias.[32,33] As a distinct feature of CAFM, both the CAFM and AFM images can be simultaneously obtained for the same area, though the AFM image owns a less spatial resolution than the DFM image. In the present study, the current compliance (CC) was set to 100 pA, and for measuring the current–voltage (I–V) curves, the time parameters for probing and waiting were set to 10 ms and 1 ms, respectively.

3. Results

3.1. Thin film characterization

As displayed in Fig. 1(a), the θ–2θ XRD patterns for all the films exhibit only the diffraction peaks from the (00l) planes, showing a pure phase and a highly (00l) orientation. Figures 1(b)–1(e) illustrate the (002) diffractions peaks obtained with a slow θ–2θ scan rate. For the thin films $\mathcal{FS}$-22 and $\mathcal{VS}$-22, the peak profiles are symmetric with clear Laue oscillations. Upon increasing the thickness, the peak profiles become asymmetric, especially for $\mathcal{FS}$-80. The peak simulation yields consistent film thickness for $\mathcal{FS}$-22 and $\mathcal{VS}$-22 [Figs. 1(b) and 1(c)], while for $\mathcal{FS}$-80 and $\mathcal{VS}$-80 it reveals two neighbouring sub-peaks [Figs. 1(d) and 1(e)]. The out-of-plane (c) lattice constants are extracted as follows: $c\sim4.007$ Å ($\mathcal{FS}$-22), $c\sim4.008$ Å ($\mathcal{VS}$-22), $c_{1,2}\sim4.000$ Å and 3.983 Å ($\mathcal{FS}$-80) and, $c_{1,2}\sim3.995$ Å and 3.983 Å ($\mathcal{VS}$-80). For bulk LSMO (space group $R\bar{3}c$) the pseudocubic lattice constant $a_p\sim3.88$ Å,[34] while for cubic LAO $a_p=3.79$ Å. In light of the observed expansion in c and the two sub-peaks in XRD, the films ($\mathcal{FS}$-22 and $\mathcal{VS}$-22) should be still largely imposed with the compressive strain, whereas for $\mathcal{FS}$-80 and $\mathcal{VS}$-80 the misfit strain has been markedly released.

The surface topography were first observed by DFM. Figures 2(a)–2(d) display the representative DFM images and the fast Fourier transform (FFT). The film $\mathcal{FS}$-22 follows a Stranski–Krastanov growth with random nanodots on the surface, while for $\mathcal{VS}$-22 the nanodots are more coherently formed. As for the thicker films, $\mathcal{FS}$-80 starts to show the crosshatch, while $\mathcal{VS}$-80 displays the dense crosshatch with ripple-like lines along [010], which yield a dumbbell-like feature in the FFT [see the inset of Fig. 2(d)].

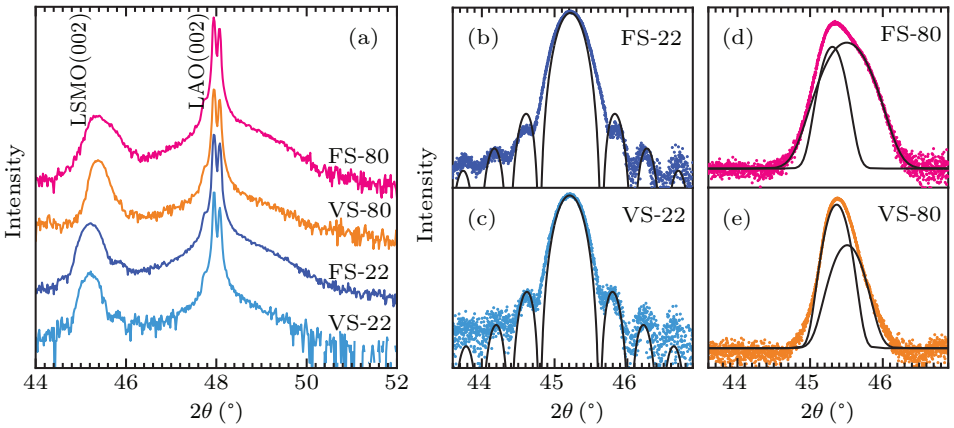


Fig. 1. (a) The θ–2θ x-ray diffraction pattern around the (002) peak of LAO(001) for the LSMO films. The slow θ–2θ x-ray diffraction scans of the (002) peaks were performed for the films $\mathcal{FS}$-22 (b), $\mathcal{VS}$-22 (c), $\mathcal{FS}$-80 (d) and $\mathcal{VS}$-80 (e). The peak profiles are simulated (solid line) for illustrating the Laue oscillations in (b), (c), and the sub-peaks in (d), (e).

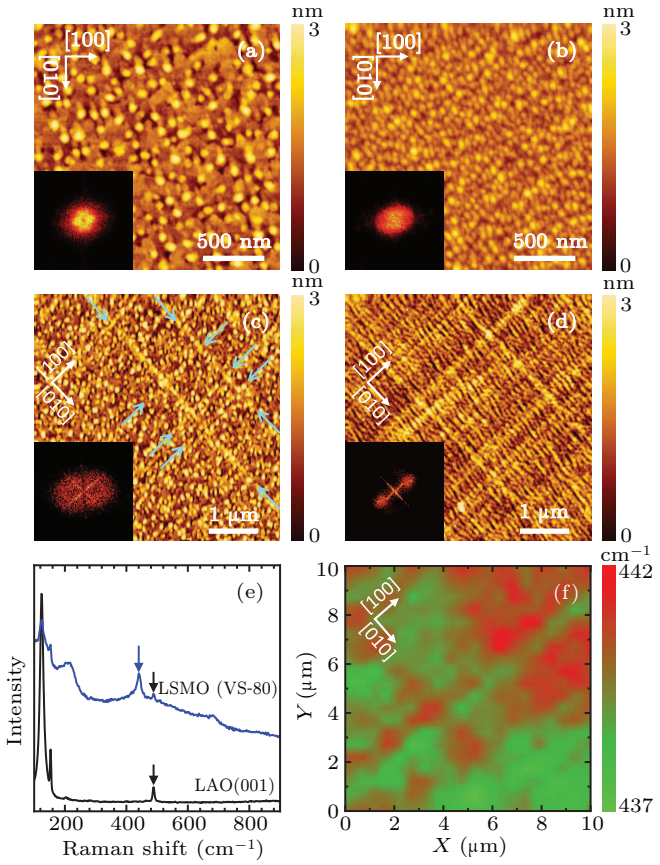


Fig. 2. The DFM images with FFT for the films $\mathcal{FS}$-22 (a), $\mathcal{VS}$-22 (b), $\mathcal{FS}$-80 (c) and $\mathcal{VS}$-80 (d). The arrows in (c) indicate the crosshatch. (e) The Raman spectra measured for the film $\mathcal{VS}$-80 (in blue) and a bare LAO(001) single crystal substrate (in black). The blue and black arrows indicate the neighboring Raman peaks from the film and the substrate, respectively. (f) The micro-Raman imaging for the film $\mathcal{VS}$-80 in terms of the bending mode at ∼440 cm^{-1}.

Figure 2(e) shows the Raman spectra measured from a random site on the surface of $\mathcal{VS}$-80. Similar to the prior work,[35–39] the spectra shows the typical phonon modes of LSMO, including the broad rotational mode at about 218 cm^{-1}, the sharp bending mode at ∼ 440 cm^{-1}, and the weak Jahn–Teller mode at ∼ 682 cm^{-1}. The phonon modes at 124 cm^{-1}, 153 cm^{-1} and 488 cm^{-1} are due to the bottom LAO single crystal, as can be seen from the spectra measured for a bare LAO(001) substrate,[35] also displayed in Fig. 2(e). Compared to the spectra of $\mathcal{VS}$-22 (Fig. S1, supplementary material), the LSMO bending mode in $\mathcal{VS}$-80 is softened at least up to 4.5 cm^{-1}, while the nearby LAO phonon mode stays nearly constant at 488.2–488.4 cm^{-1}, showing that the LSMO bending phonon mode is sensitive to the misfit strain. Hence $\mathcal{VS}$-80 was further assessed by in-plane micro-Raman imaging. As shown in Fig. 2(f), the micro-Raman graph (10×10 μm^2) in terms of the bending phonon mode also unravels a crosshatch pattern with modulation contrast up to ∼ 5 cm^{-1}.

To evaluate the chemical homogeneity, the x-ray absorption spectra at the Mn $L_{2,3}$ edges were collected with normal and 45° incidence. As shown in Fig. S2 of supplementary material, the spectra are all similar, and the peak positions are the same within the energy resolution (∼ 0.2 eV). In addition, for $\mathcal{VS}$-80, the chemical stoichiometry was further inspected by EDS. As shown in Fig. S3 of supplementary material, the SEM image shows the crosshatched surface, but no similar contrast can be seen in the EDS mapping for La, Sr and Mn. These together with the micro-Raman results confirm that the crosshatch patterns should not be associated with a chemical segregation with the cations but an in-plane undulation in the strain field.[15]

The thermomagnetization curves of $\mathcal{FS}$-80 were measured and shown in Fig. S4 of supplementary material. Due to the residual compressive strain imposed by the substrate, the Curie temperature revealed by the maximum of $-\mathrm{d}M/\mathrm{d}T$ was found to be decreased to ∼ 240 K. This hinders an *in situ* magnetic force microscopy (MFM) observation at room temperature, when the oxygen vacancies are varied locally. In the following, we focus on the CAFM studies of the LSMO films.

3.2. CAFM study of $\mathcal{FS}$-80

The CAFM studies began with $\mathcal{FS}$-80 and and mainly proceeded in this film. The measuring circuit is schematically shown in Fig. 3(a). The PtIr coated tip was grounded, acting as a mobile electrode with a front width $w_1 \sim 20$ nm. The Ag pad was prepared by curing of silver-filled epoxy adhesive, acting as a side electrode with a length $w_2 \sim 5$ mm. The voltage was applied over a distance $d \sim 1$ mm from about the film center.

After recording the pristine topography of the interested region by AFM at zero bias, the *in situ* CAFM imaging started with +2 V. As shown in Figs. 3(d) and 3(e), the AFM images obtained at 0 V and +2 V show the same topographical crosshatch, while the CAFM image [Fig. 3(b)] reveals distinct conductive dots (CDs), notwithstanding those blurred by the saturated streaks probably due to a Joule heating effect. For a clear comparison, the regional CAFM and AFM images are extracted from Figs. 3(b) and 3(e), as displayed in Figs. 4(a), 4(b), 4(c′) and 4(a′), 4(b′), 4(c), respectively, where some typical CDs and topographical dots (TDs) are outlined at their positions. It can be seen that a few CDs (e.g., series CA and CB) are lined up along [100] and [010] directions, but most other CDs are randomly distributed like CD1–CD4, and in all the cases, the CDs do not coincide with conspicuous TDs, and vice versa for the TDs (TD1–TD10) on or off the crosshatch.

Once finishing the +2 V scan, the CAFM imaging was *in situ* continued under −5 V. The crosshatch topography [Fig. 3(f)] *in situ* acquired by the AFM remains as the pristine, while the −5 V CAFM shows crosshatch of a weak current magnitude [Fig. 3(c)]. As compared in Fig. 5, for the positions of those marked topographical lines (TLs) and conductive lines (CLs), the TL/CL pairs TL8/CL7 and TL9/CL9 are found to coincide with each other, while the pairs TL1/CL1 and TL2/CL4 stay adjacently. However, TL3–TL7 and TL10 find no corresponding CLs, while for CL2, CL3, CL5, CL6, CL8 and CL10, vice versa. The spatial relation between the

CLs (CL3–CL10) and the CDs revealed by the +2 V CAFM is illustrated in Figs. 4(d) and 4(d′). One sees that some CDs appear on the CLs, but in general, they are distant from each other.

After the CAFM imaging, the local *I*–*V* response was measured by positioning the metallic tip on the single surface sites. As shown in Figs. 6(a) and 6(e), two typical sites (S_1 and S_2) at the crosshatch intersection were chosen from the contiguous regions of no measuring history. Same as before, the pristine topography [Figs. 6(a) and 6(e)] was recorded by AFM at 0 V. At S_1, the measured *I*–*V* curves show apparent hysteresis especially at the positive bias [Figs. 6(b)–6(d)]. The occurrence of threshold switching can be viewed from the current jump up/down at the critical voltages (V_t/V_h), and the back to the high resistive (HR) state before approaching 0 V.[40] As cycling to the second *I*–*V* loop (#5–#8), V_t^+ is markedly reduced, while V_h^+ is just slightly lowered. At the negative bias, the branches #7–#8 become rather close, displaying the so-called unidirectional threshold switching.[41]

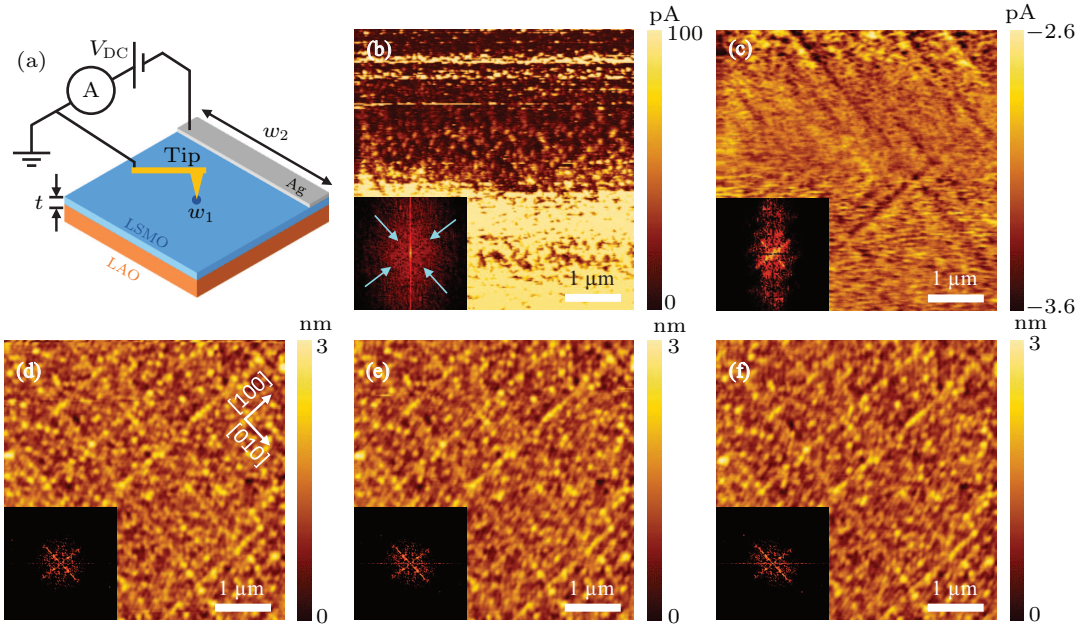


Fig. 3. The CAM study of $\mathcal{FS}$-80. (a) The schematic of the CAFM measuring circuit. The CAM images were measured at +2 V (b) and −5 V (c). The pristine AFM image (d) was measured at 0 V before the CAFM imaging. The AFM images (e) and (f) were simultaneously obtained with the CAFM imaging at +2 V and −5 V, respectively. All the CAFM and AFM images are with FFT shown in the insets. The arrows in the inset of (b) indicate the symmetry along the [100] and [010] directions.

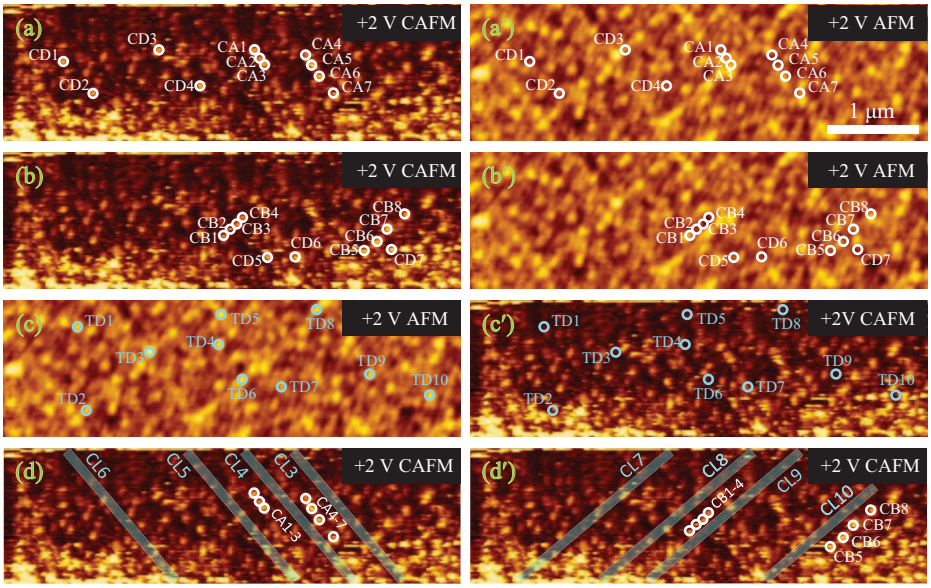


Fig. 4. For $\mathcal{FS}$-80, the comparison (regional) for the spatial relations between the conductive dots (CDs), the topographical dots (TDs), and the conductive lines (CLs). The regional +2 V CAFM (a), (b), (c′), (d), (d′) [AFM (a′), (b′), (c)] images are the same, partially extracted from that shown in Fig. 3(b) [Fig. 3(e)]. For comparing convenience, the CDs and TDs are marked out at their positions in both the CAFM and AFM images. The orthogonal CLs (d), (d′) are adopted from those marked and numbered in the −5 V CAFM imaging shown in the following Fig. 5. For a clear viewing, the CLs along [100] and [010] are shown in (d) and (d′), respectively (see the context).

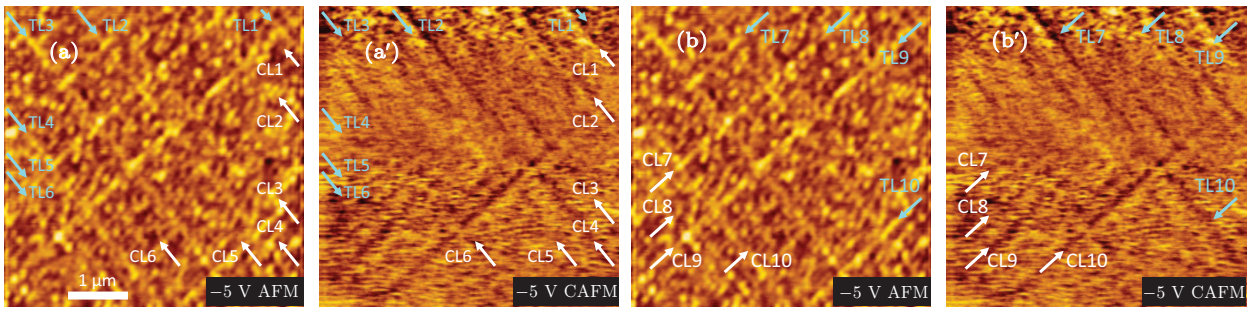


Fig. 5. For $\mathcal{FS}$-80, the comparison for the spatial relation between the topographical lines (TLs) and CLs shown in the −5 V AFM (a), (b) and CAFM (a′), (b′) images, respectively. For comparing convenience, the TLs and CLs are marked out in both the AFM and CAFM images. Note that the CAFM (AFM) images are the same, re-plotted from Fig. 3(c) (Fig. 3(f)). The TLs and CLs along [100] and [010] are shown in (a), (a′) and (b), (b′), respectively (see the context).

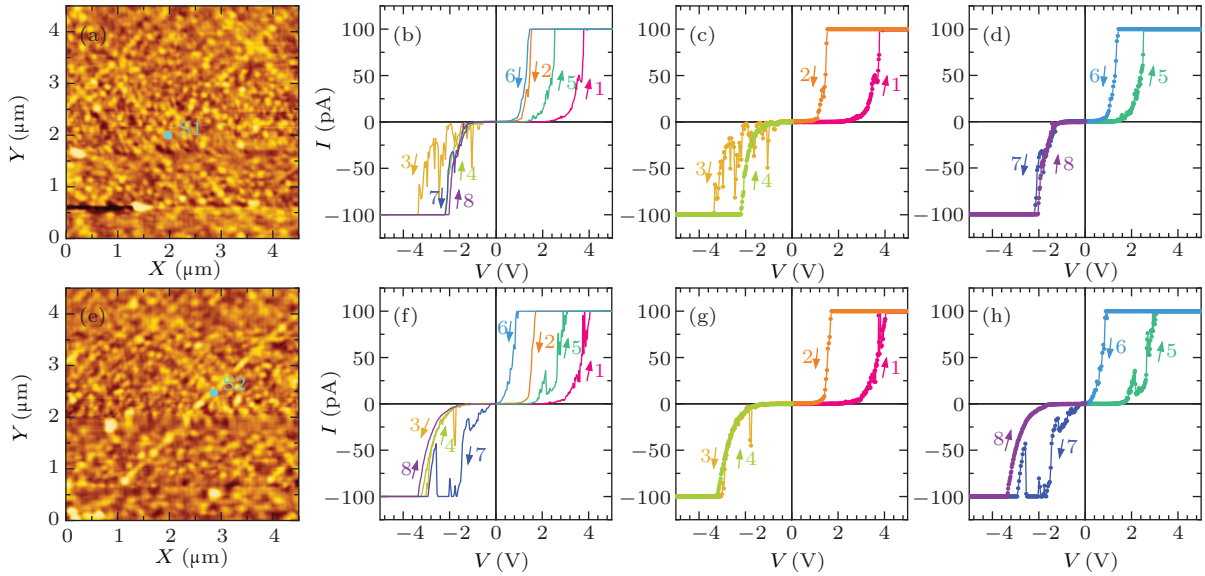


Fig. 6. The local *I*–*V* measurements at the surface sites S_1 (a), (b) and S_2 (e), (f) in $\mathcal{FS}$-80: The sites S_1 (a) and S_2 (e) are marked out in the AFM images recorded before measuring the *I*–*V* response. Note that, the *I*–*V* curves are consecutively measured at each site from branch #1 to #8. For a clear viewing, the first (#1–#4) and second (#5–#8) *I*–*V* loops are separately plotted in (c), (g) and (d), (h). The arrows indicate the sweeping direction.

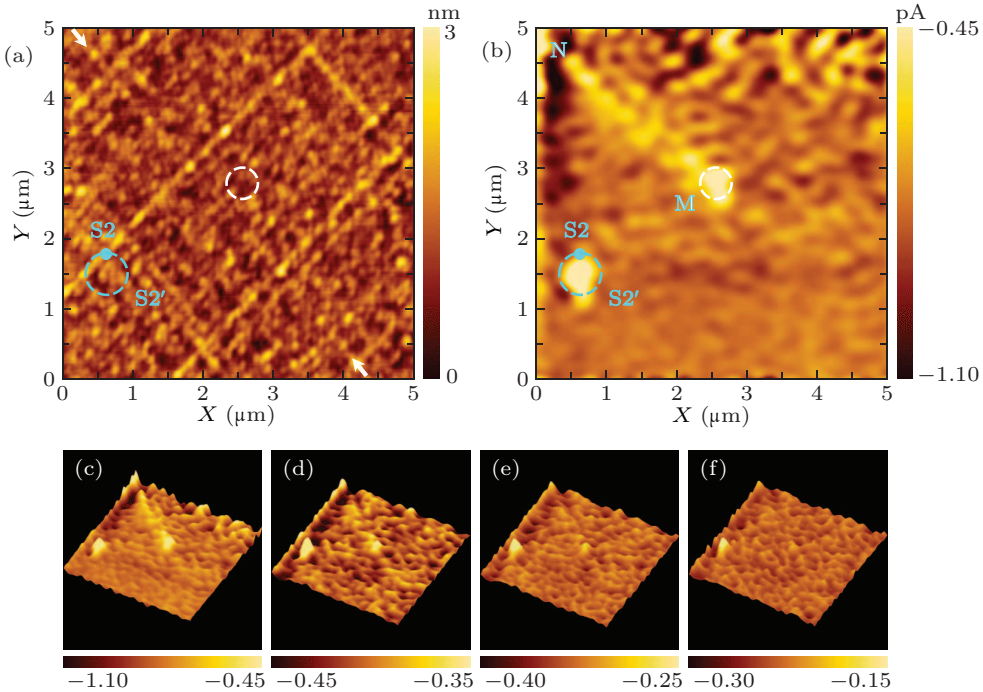


Fig. 7. For $\mathcal{FS}$-80, the simultaneous AFM (a) and CAFM imaging (b) at −5 V in the region including the site S_2 just after finishing the *I*–*V* measurements. The positions for the emerged CDs at S2′ and at about the imaging center M are marked out by dashed circles. The emerged CL along the half diagonal is denoted by MN. The arrows in (a) indicate the light TL adjacent to the feature of MN along the half diagonal. (c)–(f) The CAFM imaging at −5 V, consecutively scanned from (c) to (d), (e), and (f).

For the *I*–*V* response at S_2 [Figs. 6(f)–6(h)], the measured *I*–*V* branches #1–#3 are rather similar to that measured at S_1, in terms of the threshold switching at the similar critical voltages. In contrast, the hysteresis between the branches #3 and #4 becomes less, enabling an earlier occurrence of unidirectional threshold switching in the first *I*–*V* loop. Furthermore, the second loop (#5–#8) shows the bipolar memristive switching,[42] i.e., applying positive and negative voltages results in the low resistive (LR) and HR states at 0 V, respectively. Just after completing the last *I*–*V* measurement (#8: -10 V$\rightarrow$0 V), the neighbouring region including S_2 was imaged by AFM and CAFM at -5 V. As shown in Fig. 7(a), the crosshatch topography remains unchanged. In the CAFM image [Fig. 7(b)], however, there emerge a HR dot at S_2', a HR dot at about the imaging center (M), and a HR segment (MN) along the half diagonal. The site of S_2' is quite close to S_2, while the spontaneous feature of MN finds no clear topographical counterpart except one light neighboring TL indicated by the arrows in Fig. 7(a). Notably, upon repeating the CAFM imaging [Figs. 7(c)–7(f)], the HR state at S_2' keeps stable, whereas the MN segment fades somewhat faster than the central HR dot at M.

3.3. CAFM study of $\mathcal{VS}$-80

Following the work with $\mathcal{FS}$-80, the CAFM study for $\mathcal{VS}$-80 started directly from measuring the local *I*–*V* property. Note that the crosshatch is dense in this film. The *I*–*V* curves were probed at the arbitrary points (P_1, P_2) in the contiguous regions of no measuring history, as shown in Figs. 8(a), 8(b) and 8(e), 8(f), respectively. The pristine topography shown in Figs. 8(a) and 8(e) were also recorded by AFM at 0 V before measuring the *I*–*V* curves. At P_1, the first *I*–*V* hysteresis loop (#1–#4) shows threshold switching in both positive and negative bias [Fig. 8(c)]. In the second *I*–*V* loop (#5–#8), while V_t^+ remains almost unchanged, V_h^+ is much decreased so that there follows a nonvolatile LR state at zero bias, though which later switches back to the HR state with a minor negative voltage [Fig. 8(d) and the inset]. At P_2, the bipolar memristive switching shows early in the first *I*–*V* loop [Fig. 8(g)]. Upon measuring to the second *I*–*V* loop [Fig. 8(h)], there unexpectedly recovers the threshold switching with both $V_{t,h}^+$ close to that of the second *I*–*V* loop measured at P_1.

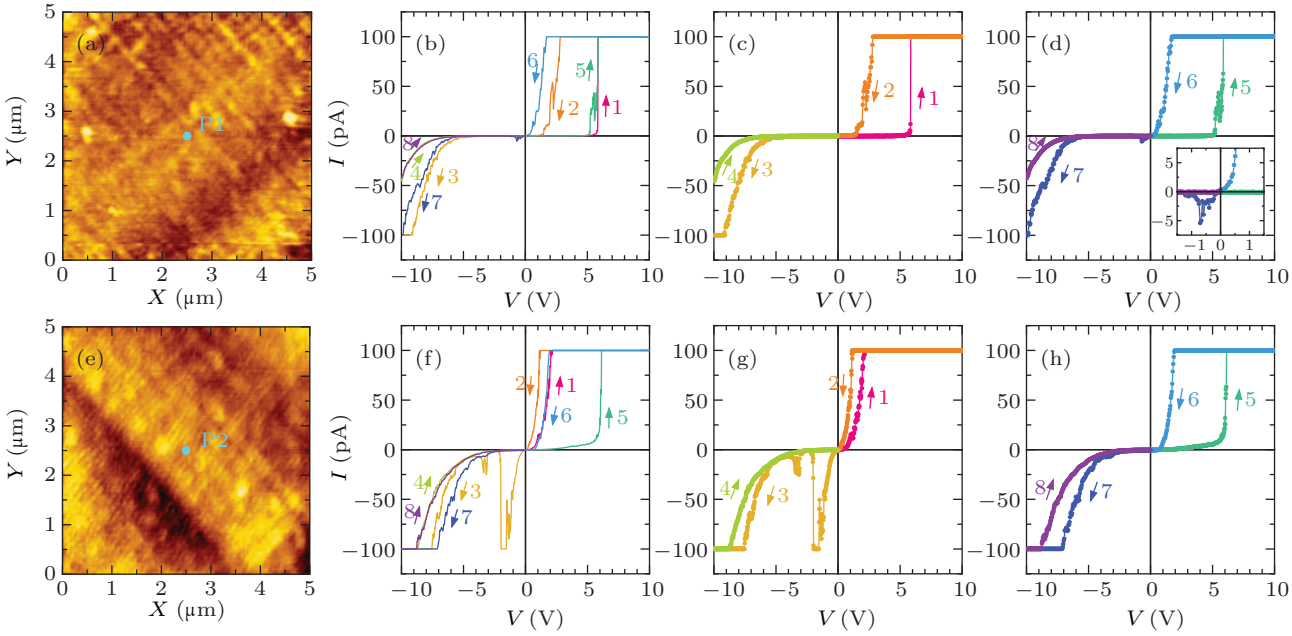


Fig. 8. The local *I*–*V* measurements at the surface sites P_1 (a), (b) and P_2 (e), (f) in $\mathcal{VS}$-80. The sites P_1 (a) and P_2 (e) are selected from the arbitrary points about at the center of the AFM image, recorded before the *I*–*V* measurements. The *I*–*V* curves were consecutively measured at each site from branch #1 to #8. For a clear viewing, the first (#1–#4) and second (#5–#8) loops are separately plotted in (c), (g) and (d), (h). The inset of (d) zooms in the low bias regime. The arrows indicate the sweeping direction.

Like the prior study at S_2 for $\mathcal{FS}$-80, once finishing the last *I*–*V* measurement (#8: -10 V$\rightarrow$0 V) at P_2, its neighbouring region including P_2 was imaged by AFM and CAFM. As shown in Figs. 9(a) and 9(b), the topography at P_2 is changed into a hillock, around which the local area (CD1) on a expanded scale is switched into the HR state. Meanwhile, other two HR spots (CD2, CD3) exhibit at about the imaging center along the [100] direction. Compared to the HR segment of MN shown in $\mathcal{FS}$-80, these emerged HR features including that (CD1) around P_2 are all proved to be stable against the consecutive imaging (Fig. S5, supplementary material). In the CAFM image [Fig. 9(b)], one can also see the CLs, though a bit vague. As partially marked out by the arrows, they are largely along [100], the atomic step edge direction for the vicinal substrate, while only a few are along the perpendicular direction. Among them, some CL and TL stay close (e.g., CL2/TL3, CL6/TL6), but the rest however show no clear correlation.

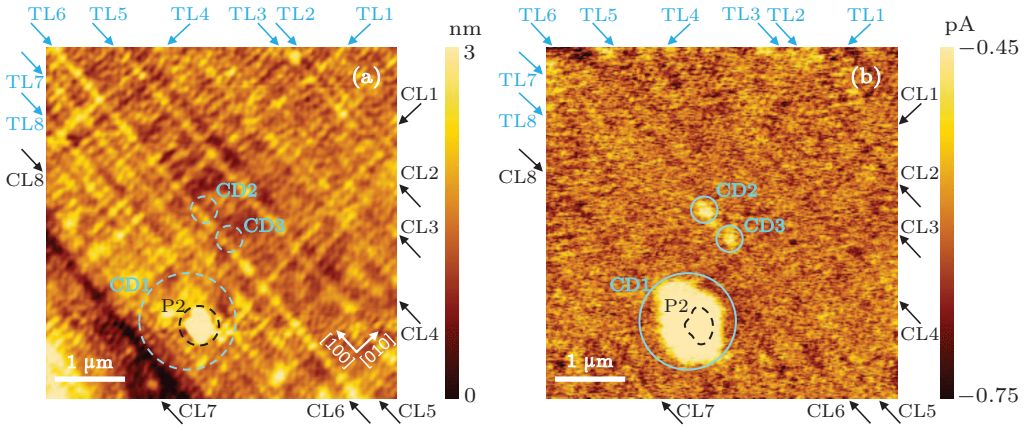


Fig. 9. For $\mathcal{VS}$-80, the simultaneous AFM (a) and CAFM imaging (b) at −5 V in a nearby region including the site P_2 just after finishing the *I*–*V* measurements. For assessing the spatial relation, the emerged TD at P_2, and the emerged CDs including CD1 around P_2, and CD2,3 at about the image center are all circled, and meanwhile, some TLs and CLs are identified by arrows in both the AFM and CAFM images.

4. Discussion

Accompanied with imperfections in heteroepitaxy, dislocation half-loops generally nucleate at epilayer surface. As the growth proceeds they penetrate downwards, and bend into the misfit dislocations that can be mostly down to the film–substrate interface.[43] From another perspective, dislocations can not end within a crystal but terminate at free surface through threading dislocations, due to the conservation of Burgers vector. In principle, misfit dislocations play the dominant role in strain relaxation. Hence, to release the misfit strain in a thicker epilayer, more misfit dislocations are generated, which can be self-organized into ordered networks by the enhanced interactions between dislocations and dislocation dipoles. Note that, misfit dislocations are usually orient along the low indexed crystallographic directions. They thus readily enable long-range ordered undulations in the surface potential, which leads to the topographical crosshatch by resulting in a preferential adatom diffusion on the epilayer.

Given that, the dislocations in the present films allow the preferential location and also the faster diffusion of oxygen vacancies,[25–27] the ionic conduction could be prominent if both electrodes contact the dislocation network. The macro-sized Ag electrode meets the requirement through contacting the threading dislocations, and, they in fact together form a virtual cathode as pointed out by Waser *et al.*[6] By contrast, the front of the scan tip has a radius of $\sim$ 10 nm while the core of an edge-type dislocation is in a scale of $\sim$ 1–2 nm.[19,44–46] Therefore, as illustrated in Fig. 10, the measured CAFM signal should critically rely on the quantity and penetration depth of the threading dislocations under the mobile tip.

In the study of $\mathcal{FS}$-80, when the CAFM imaging was performed at +2 V, the oxygen vacancies originally absorbed in the threading dislocations are repelled downwards, which sets the conductive channels between the threading dislocations and the virtual cathode, thus enabling the threading dislocations manifested as CDs out of the insulating matrix [Fig. 3(b)]. Owing to the chemical expansion effect,[47] the pipe diffusion of oxygen vacancies along the threading dislocations should be impeded by the residual compressive strain which increases with the penetration depth. In other words, the brighter CDs should correspond to the shallower threading dislocations. In the −5 V CAFM imaging, the oxygen vacancies are attracted towards the metal (tip)–oxide interface. But when the scan tip laterally approaches the threading dislocation, the oxygen vacancies from underneath are mainly attracted to the threading dislocation cores due to the limited dwelling time for each scan step. This makes the outer edge region slightly more conductive, as where the local strain is still more relaxed than the insulating matrix. Moreover, depending on the local quantity of the threading dislocations that follow the misfit dislocation order, the conductive outer edge of the former can be connected along the surface,[19] thus forming a weak contrast of crosshatch in the CAFM image. This dynamic vacancy behavior also explains why there are only a few CDs along the crosshatch direction.

As for the TLs showing no features in the corresponding CAFM image, they should mostly associated with the long range ordered misfit dislocations down to the LSMO–LAO interface, because the outer edge of the connected threading dislocations should be more insulating with increasing the penetrating depth. It can be inferred that the CLs not matching any topographical features should be attributed to the up most dislocations which are created close to the final growth stage, and thus have no sufficient time to form any related TLs. For those TL–CL pairs that coincide or stay close with each other, their spatial relation can be understood as follows: If the lines are perpendicular to the length of the Ag electrode, the outer edge conduction is symmetric to the core of threading dislocations, thereby the central positions of the CL and TL are well matched. Otherwise, if the lines are parallel to the length of the Ag electrode, the outer edge conduction turns a bit asymmetric to the core of the threading dislocations. The higher conduction at the lower left side lets the observed CL stay in neighbouring to the TL.

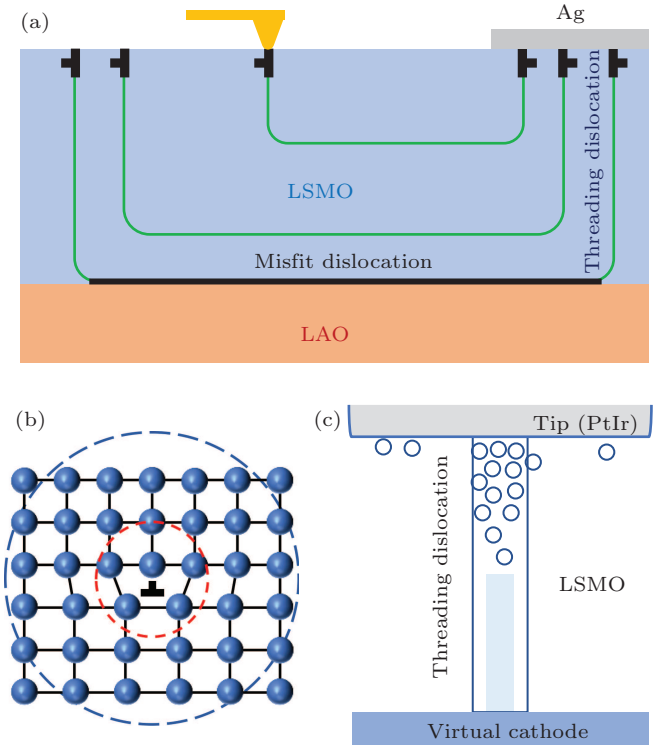


Fig. 10. The schematics for (a) the dislocation half-loops, misfit and threading dislocations created in heteroepitaxy; (b) the core structure of an edge-type dislocation; and (c) the conduction between the metallic tip (PtIr) and the virtual cathode through a threading dislocation, in which the top region initially attracts more oxygen vacancies.

On the other hand, it should not be accidental that all the HR dots (M, CD2, CD3) emerge at about the image center, because another similar event was also observed later for $\mathcal{FS}$-80 (Fig. S6, supplementary material). Note that the CAFM imaging proceeds from left to right and, top to bottom. Once scanned in negative bias, the current paths along the dislocation network in the half diagonal direction would be largely blocked due to the attracted oxygen vacancies. The current instead chooses to flow along the paths in the unprobed area. Upon the cumulative scan, the central region of the imaging square should bear the most current processing, which promotes the local memristive switching to the HR dot. For $\mathcal{FS}$-80, the MN segment is mainly attributed to a presence of the shallow misfit and threading dislocations. For $\mathcal{VS}$-80, the CLs observed in Fig. 9(b) are also ascribed to the shallower dislocations but which would be aligned with some structural boundaries parallel to the atomic step edge direction for the vicinal substrate.[30,48] In principle, the atomic steps on the vicinal LAO(001) reduce the fourfold surface symmetry into twofold. This symmetry reduction is expected to induce an anisotropic strain in the film plane, which in turn results in a modulation in the configurations of dislocations and oxygen vacancies. Compared to the feature of MN in $\mathcal{FS}$-80, the HR dots (CD2, CD3) for $\mathcal{VS}$-80 appear more stable. The better endurance suggests that the oxygen vacancies in the latter films should be more correlated owing to the influence from the vicinal substrate.

To gain further insight into the oxygen-vacancy dynamics, the local I–V characteristics are analyzed. Among the models describing the charge transport in semiconductor heterodevices, the Poole–Frenkel emission (PFE) is a typical bulk-limited conduction, referring to a mechanism in which the charge carriers initially trapped by the defects in the semiconductor, can be detrapped to the conduction band upon external electric field that lowers the Coulomb potential barrier.[49] This conduction yields the current density as

$$J = q\mu E N_{\mathrm{C}} \exp\left[\frac{-q(\phi_{\mathrm{B}} - \sqrt{qE/\pi\varepsilon_0\varepsilon_{\mathrm{r}}})}{k_{\mathrm{B}}T}\right], \tag{1}$$

where q is the electron charge, μ is the field independent carrier mobility, N_{C} the density of states in the conduction band, E the electric field, ε_0 the permittivity of free space, ε_{r} the relative permittivity, ϕ_{B} the depth of the trap potential well, k_{B} the Boltzmann constant, and T the absolute temperature. Compatible with this mechanism, the dislocations in the LSMO films serve as the essential defects, naturally enabling the initial correlated or clustered oxygen vacancies. Furthermore, in contrast to other models for bulk limited conduction, the PFE modeling yields a sensible physical parameter, i.e., the optical dielectric constant, as

$$\varepsilon_{\mathrm{r}} = \frac{q^3}{\pi\varepsilon_0\eta^2 {k_{\mathrm{B}}}^2 T^2}, \tag{2}$$

where η is the slope for the linearity of the PFE plot, i.e., $\ln J/E$ vs. $\sqrt{E}$ based on Eq. (1).

In this context, considering that the oxygen vacancies are attracted to the contacted tip in negative bias, we take the representative I–V branches #4 and #8 for fitting the PFE formula. Figure 11 displays the plots of $\ln J/E$ vs. $(-E)^{1/2}$, where $E = V/t_{\mathrm{eff}}$, and t_{eff}, the effective depth from the metallic tip down to the virtual cathode is assigned to a full thickness of 80 nm. It can be seen that the linear fit applies sectionally or to one wide field regime before approaching CC. The corresponding dielectric constants are calculated from the linear slopes by using Eq. (2), as listed in the plots.

In the case of S_1, $\varepsilon_{\mathrm{r}} \sim 7.10$ (#4), and $\varepsilon_{\mathrm{r}} \sim 3.67$ (#8) in the low field regime, are at a similar level with the values $\varepsilon_{\mathrm{r}} \sim 4$–4.8 in bulk LSMO[50,51] and $\varepsilon_{\mathrm{r}} \sim 3.39$–6.05 in polycrystalline LSMO films.[52] In the high field regime, $\varepsilon_{\mathrm{r}} \sim 1.99$ (#4) and $\varepsilon_{\mathrm{r}} \sim 0.68$ (#8) are much less, and in particular the latter seems unphysically small. If having these two ε_{r}s larger than 3 by assuming a smaller depth to t_{eff}, the low field ε_{r} turns to exceed 11, which is much higher than the reported ε_{r}s. This incongruity implies that the low field conduction at S_1 may obey the PFE mechanism with a few clustered oxygen vacancies, but the conduction in high fields would be involved with some other charge transport process.[49]

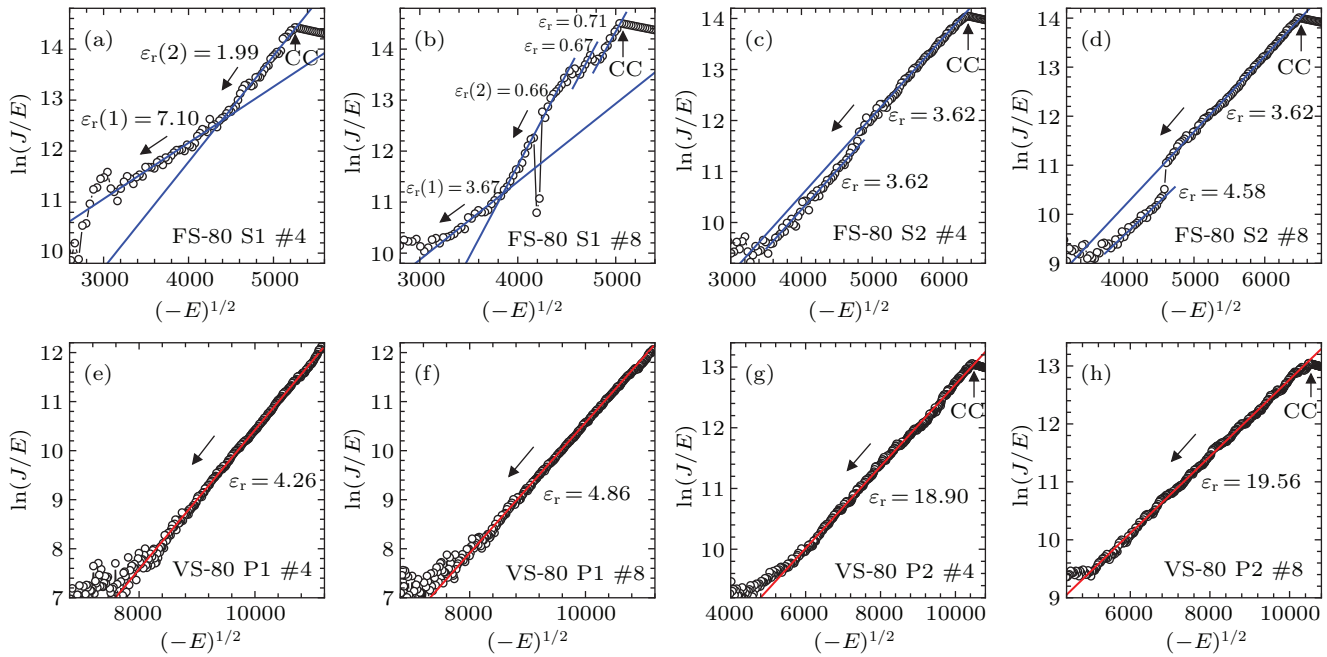


Fig. 11. $\ln(J/E)$ plotted vs. $(-E)^{1/2}$ corresponding to the *I*–*V* branches #4 and #8 measured at S_1 (a), (b) and S_2 (c), (d) for $\mathcal{FS}$-80, and at P_1 (e), (f) and P_2 (g), (h) for $\mathcal{VS}$-80. The current compliance is denoted by CC. The lines are fits to the PFE mechanism. The dielectric constants ε_r are calculated from the linear slopes based on Eq. (2). The arrows indicate the sweeping direction.

In the case of S_2, $\varepsilon_r \sim 3.62$ (#4), $\varepsilon_r \sim 4.58$–3.62 (#8); and for P_1, $\varepsilon_r \sim 4.26$ (#4), $\varepsilon_r \sim 4.86$ (#8). They are similar to the reported ε_rs. Among the cases, the extracted ε_rs appear a bit larger at P_1, showing that this site initially traps more oxygen vacancies than S_1. Meanwhile, at both S_2 and P_1, ε_rs appear to be slightly increased from branch #4 to #8. This tendency suggests an evolution picture, consistent with the model proposed in our prior work,[53] namely, upon field cycling, some clustered oxygen vacancies that are initially inactive and locate deep in the threading dislocations can be decoupled into smaller clusters and single vacancies, which progressively enrich the vacancy density at the metal (tip)–oxide interface. Also with this picture, the expanded HR dot S_2' forming just in the vicinity of S_2 could be ascribed to a presence of more threading dislocations at S_2', where the absorbed clusters of oxygen vacancies can be decoupled and then attracted to the probed surface in the subsequent CAFM imaging only after being triggered by the memristive switching at S_2.

As for the case at P_2, the extracted $\varepsilon_r \sim 18.90$ (#4) and $\varepsilon_r \sim 19.56$ (#8) are far beyond the reported values. They imply that this site should contain more threading dislocations, thus initially attracting oxygen vacancies even more than at P_1, and allowing the earlier occurrence of memristive switching. On the other side, the topographical change at this site suggests a possible formation of excessive oxygen bubbles under the positively charged tip, which causes the localized deformation and/or decomposition,[45,54,55] as well as the back to the threshold switching. By recalling the RS senarios at the sites $S_{1,2}$ and P_1, it can be deduced that, transformation from threshold to memristive switching requires the adequacy of active oxygen vacancies, but, as indicated by the case at P_2, an excess of oxygen vacancies is adverse to a mild and durable memristive switching.

5. Conclusion

To summarize, we have revealed the conductive path and the local oxygen-vacancy dynamics in crosshatched LSMO films through analyzing a variety of CAFM and AFM imaging, and local *I*–*V* measurements. The results demonstrate that the side Ag pad together with the dislocation network forms the virtual cathode. Owing to the long-range ordered undulations in the in-plane stain field, crosshatch and aligned dot features show in both AFM and CAFM, but in these two channels they are not all necessarily in a one-to-one mapping relation, indicating a depth distribution of the dislocations and oxygen vacancies. The local *I*–*V* measurements further unravel that the occurrence of threshold and memristive switching are closely associated with the local profile and concentration of oxygen vacancies, which are modulated by both the threading and misfit dislocations. Note the present LSMO/LAO systems of compressive strain, the crosshatched films with tensile strain would have further implications for the local oxygen-vacancy dynamics. This together with the MFM observation below room temperature is yet an interesting topic awaiting a future study.

Acknowledgements

Z. H. W. wishes to thank K. Zhu, Y. L. Liu, J. H. Yin and S. L. He for their help in this study. This work was funded by the Science Center of the National Science Foundation of China (Grant No. 52088101), the National Natural Science Foundation of China (Grant Nos. 11474342 and

11174353), the National Key Research and Development Program of China, and the Strategic Priority Research Program B of the Chinese Academy of Sciences. This work was also supported in part by the beamline 08U1A of SSRF.

References

[1] Kalinin S V and Spaldin N A 2013 *Science* **341** 858
[2] Schmitt R, Spring J, Korobko R and Rupp J L M 2017 *ACS Nano* **11** 8881
[3] Wang Z H, Zhang Q H, Gregori G, Cristiani G, Yang Y, Li X, Gu L, Sun J R, Shen B G and Habermeier H U 2018 *Phys. Rev. Mater.* **2** 054412
[4] Hus S M, Ge R, Chen P, Liang L, Donnelly G E, Ko W, Huang F, Chiang M, Li A and Akinwande D 2021 *Nat. Nanotech.* **16** 58
[5] Sawa A 2008 *Mater. Today* **11** 28
[6] Waser R, Dittmann R, Staikov G and Szot K 2009 *Adv. Mater.* **21** 2632
[7] Slesazeck S and Mikolajick T 2019 *Nanotechnology* **30** 352003
[8] Wang Z, Wu H, Burr G W, Hwang C S, Wang K L, Xia Q and Yang J J 2020 *Nat. Rev. Mater.* **5** 173
[9] Ielmini D and Wong H S P 2018 *Nat. Electron.* **1** 333
[10] Sangwan V K and Hersam M C 2020 *Nat. Nanotech.* **15** 517
[11] Asif M and Kumar A 2022 *Mater. Today Electron.* **1** 100004
[12] Kishinô S, Ogirima M and Kurata K 1972 *J. Electrochem. Soc.* **119** 617
[13] Chang K H, Gilbala R, Srolovitz D J, Bhattacharya P K and Mansfield J F 1990 *J. Appl. Phys.* **67** 4093
[14] Hsu J W P, Fitzgerald E A, Xie Y H, Silverman P J and Cardillo M J 1992 *Appl. Phys. Lett.* **61** 1293
[15] Chen H, Li Y K, Peng C S, Liu H F, Liu Y L, Huang Q, Zhou J M and Xue Q K 2002 *Phys. Rev. B* **65** 233303
[16] Rovaris F, Zoellner M H, Zaumseil P, Marzegalli A, Di Gaspare L, De Seta M, Schroeder T, Storck P, Schwalb G, Capellini G and Montalenti F 2019 *Phys. Rev. B* **100** 085307
[17] Sánchez F, Lüders U, Herranz G, Infante I C, Fontcuberta J, Garcüa-Cuenca M V, Ferrater C and Varela M 2005 *Nanotechnology* **16** S190
[18] Kim S G, Wang Y and Chen I W 2006 *Appl. Phys. Lett.* **89** 031905
[19] Wang Z H, Lebedev O I, Van Tendeloo G, Cristiani G and Habermeier H U 2008 *Phys. Rev. B* **77** 115330
[20] Park S, Ryan P, Karapetrova E, Kim J W, Ma J X, Shi J, Freeland J W and Wu W 2009 *Appl. Phys. Lett.* **95** 072508
[21] Tan X L, Chen F, Chen P F, Xu H R, Chen B B, Jin F, Gao G Y and Wu W B 2014 *AIP Advances* **4** 107109
[22] Metlenko V, Ramadan A H H, Gunkel F, Du H, Schraknepper H, Hoffmann-Eifert S, Dittmann R, Waserb R and De Souza R A 2014 *Nanoscale* **6** 12864
[23] Marrocchelli D, Sun L and Yildiz B 2015 *J. Am. Chem. Soc.* **137** 4735
[24] Waldow S P and De Souza R A 2016 *ACS Appl. Mater. Interfaces* **8** 12246
[25] Bagués N, Santiso J, Esser B D, Williams R E A, McComb D W, Konstantinovic Z, Balcells L and Sandiumenge F 2018 *Adv. Funct. Mater.* **28** 1704437
[26] Navickas E, Chen Y, Lu Q, Wallisch W, Huber T M, Bernardi J, Stöger-Pollach M, Friedbacher G, Hutter H, Yildiz B and Flei J 2017 *ACS Nano* **11** 11475
[27] Börgers J M, Kler J, Ran K, Larenz E, Weirich T E, Dittmann R and De Souza R A 2021 *Adv. Funct. Mater.* **31** 2105647
[28] Liang Z W, Wang Z H, Feng Y, Zhang Q H, Wang L C, Wang C, Gu L, Wu P and Shen B G 2019 *Phys. Rev. B* **99** 064304
[29] Wang Z H, Cristiani G and Habermeier H U 2003 *Appl. Phys. Lett.* **82** 3731
[30] Haage T, Zegenhagen J, Li J Q, Habermeier H U, Cardona M, Jooss C, Warthmann R, Forkl A and Kronmüller H 1997 *Phys. Rev. B* **56** 8404
[31] Wang L C, Wang Z H, He S L, Li X, Lin P T, Sun J R and Shen B G 2012 *Physica B* **407** 1196
[32] Schirmeisen A, Anczykowski B and Fuchs H 2005 *Nanotribology and Nanomechanics* edited by Bhushan B (Heidelberg: Springer) p. 235
[33] Rodenbücher C, Wojtyniak M and Szot K 2019 *Electrical Atomic Force Microscopy for Nanoelectronics* (Leuven: Springer) p. 29
[34] Wu Y, Suzuki Y, Rüdiger U, Yu J, Kent A D, Nath T K and Eom C B 1999 *Appl. Phys. Lett.* **75** 2295
[35] Bormann D, Desfeux R, Degave F, Khelifa B, Hamet J F and Wolfman J 1999 *Phys. Stat. Sol. (B)* **215** 691
[36] Dediu V A, López J, Matacotta F C, Nozar P, Ruani G, Zamboni R and Taliani C 1999 *Phys. Stat. Sol. (B)* **215** 625
[37] Li T, Wang B, Dai H, Du Y, Yana H and Liu Y 2005 *J. Appl. Phys.* **98** 123505
[38] Dore P, Postorino P, Sacchetti A, Baldini M, Giambelluca R, Angeloni M and Balestrino G 2005 *Eur. Phys. J. B* **48** 255
[39] Merten S, Bruchmann-Bamberg V, Damaschke B, Samwer K and Moshnyaga V 2019 *Phys. Rev. Mater.* **3** 060401(R)
[40] Chang S H, Lee J S, Chae S C, Lee S B, Liu C, Kahng B, Kim D W and Noh T W 2009 *Phys. Rev. Lett.* **102** 026801
[41] Guo M Q, Chen Y C, Lin C Y, Chang Y F, Fowler B, Li Q Q, Lee J and Zhao Y G 2017 *Appl. Phys. Lett.* **110** 233504
[42] Nian Y B, Strozier J, Wu N J, Chen X and Ignatiev A 2007 *Phys. Rev. Lett.* **98** 146403
[43] Matthews J W and Blakeslee A E 1974 *J. Cryst. Growth* **27** 118
[44] Sandiumenge F, Bagués N, Santiso J, Paradinas M, Pomar A, Konstantinovic Z, Ocal C, Balcells L, Casanove M and Martínez B 2016 *Adv. Mater. Interfaces* **3** 1600106
[45] Szot K, Speier W, Bihlmayer G and Waser R 2006 *Nat. Mater.* **5** 312
[46] Hull D and Bacon D J 2011 *Introduction to Dislocations* (New York: Elsevier)
[47] Aschauer U, Pfenninger R, Selbach S M, Grande T and Spaldin N A 2013 *Phys. Rev. B* **88** 054111
[48] Djupmyr M, Cristiani G, Habermeier H U and Albrecht J 2005 *Phys. Rev. B* **72** 220507(R)
[49] Sze S M and Ng K K 2007 *Physics of Semiconductor Devices* (New Jersey: John Wiley & Sons, Inc.)
[50] Shimazaki K, Tachikawa S, Ohnishi A and Nagasaka Y 2001 *Int. J. Thermophys.* **22** 1549
[51] Fan D, Li Q and Xuan Y 2011 *Int. J. Thermophys.* **32** 2127
[52] Tikhii A A, Kara-Murza S V, Nikolaenko Y M, Gritskikh V A, Korchikova N V and Zhikharev I V 2015 *Inorg. Mater.* **51** 928
[53] Wang Z H, Yang Y, Gu L, Habermeier H U, Yu R C, Zhao T Y, Sun J R and Shen B G 2012 *Nanotechnology* **23** 265202
[54] Yang J J, Miao F, Pickett M D, Ohlberg D A A, Stewart D R, Lau C N and Williams R S 2009 *Nanotechnology* **20** 215201
[55] Wojtyniak M, Szot K, Wrzalik R, Rodenbücher C, Roth G and Waser R 2013 *J. Appl. Phys.* **113** 083713